FRONTIERS OF PHYSICS

RESEARCH ARTICLE
Volume 17 / Issue 6 / 62501 / 2022

Digital coding transmissive metasurface for multi-OAM-beam

Si Jia Li[1,2,3,†], Zhuo Yue Li[1], Guo Shai Huang[1], Xiao Bin Liu[1], Rui Qi Li[2], Xiang Yu Cao[1,3]

1 Information and Navigation College, Air Force Engineering University, Xi'an 710077, China
2 State Key Laboratory of Millimeter Waves, School of Information Science and Engineering, Southeast University, Nanjing 210096, China
3 Shaanxi Key Laboratory of Artificially-Structured Functional Materials and Devices, Air Force Engineering University, Xi'an 710051, China
Corresponding author. E-mail: †lsj051@126.com
Received March 9, 2022; accepted May 16, 2022

ABSTRACT

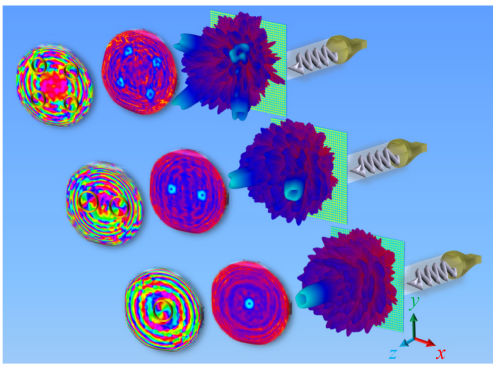

Orbital angular momentum (OAM) is a phenomenon of vortex phase distribution in free space, which has attracted enormous attention in theoretical research and practical application of wireless communication systems due to its characteristic of infinitely orthogonal modes. However, traditional methods generating OAM beams are bound to complex structure, large device, multiple layers, complex feed networks, and limited beams in microwave range. Here, a digital coding transmissive metasurface (DCTMS) with a single layer substrate and the bi-symmetrical arrow is proposed and designed to generate multi-OAM-beam based on Pancharatnam–Berry (PB) phase principle. The 3-bit phase response can be realized by encoding the geometric phase into rotation angle of unit cell for DCTMS. Additionally, the phase compensation of the metasurface is introduced to achieve the beam focusing and the conversion from spherical wave to plane wave. According to the digital convolution theorem, the far-field patterns and near-field distributions of multi-OAM-beam with $l = -2$ modes are adequately demonstrated by DCTMS prototypes. The OAM efficiency and the purity are calculated to demonstrate the excellent multi-OAM-beam. The simulated and experimental results illustrate their performance of OAM beams. The designed DCTMS has profound application in multi-platform wireless communication systems and the multi-channel imaging systems.

Keywords transmissive metasurface, orbital angular momentum, Pancharatnam–Berry phase, multi-beam, phase compensation

1 Introduction

Orbital angular momentum (OAM) is a phenomenon of electromagnetic vortex which exhibits the characteristic of vortex phase wavefront in free space [1–3]. It has infinite number of OAM modes and the different modes are orthogonal to each other. Theoretically, the vortex beam can infinitely increase the communication capacity and provide well conditions for multi-platform wireless information systems. In the last decade, plenty of methods have been proposed to generate OAM beam such as antenna array, single-chip antenna, spiral phase plate, and annular traveling wave antenna [4–7]. Nevertheless, the existing methods hardly satisfy the actual demands of wireless systems due to the disadvantages of complex structure, large device, multilayers, complex feed networks and limited beams.

Metasurface is a two-dimensional and artificial

Higher Education Press

https://doi.org/10.1007/s11467-022-1179-9

micro-structure with periodic or non-periodic arrangement, which has the characteristics of low loss, low cost and high integration in actual application [8–18]. It has diversity forms and numerous functions in manipulation of EM waves. Such functions of polarization conversion, radar cross section reduction, scattering diffusion, high isolation and beam regulation have already achieved by using the reflective and transmissive metasurface [19–21]. Nowadays, digital coding metasurface has been proposed to realize more functions [22–38]. The metasurface can simplify the design process and optimization procedure by disperse EM parameters as the elements, which could realize the multi-function by designing coding sequence on the two-dimension [22, 23]. It is reported that metasurface has already successful application in beam scattering, polarization conversion, real-time imaging and so on [24–34]. Furthermore, metasurface has also been applied to generate OAM beams [30–38]. There are two types of methods for vortex beam generation by metasurface with reflection and transmission. In fact, the reflective and incident EM waves are in the same half space [30–38]. For example, a single layer reflective metasurface has been realized to effectively generate dual-OAM-beam based on geometry phase. Meanwhile the continuous reflective phase shift is achieved by regulating length and distance of patches [35]. The multiple OAM with 1, 2, 3 and 4 beams are presented for the Gaussian beam incidences which can manipulate superpositions in multiple channels in terahertz band [36]. Moreover, the convolution theorem of reflective metasurface is proposed and demonstrated for achieving multi-function which provides the theoretical foundation for multi-beam [37]. It is necessary to note that the reflective metasurface has disadvantage of the change of propagation path for EM waves and the occlusion effect, which can hardly be applied in communication system extensively. By contrast, the transmissive metasurface naturally compensates the occlusion effect and has potential in applications. The transmissive metasurface needs to optimize more parameters for excellent performance [39–45]. Consequently, it is a big challenge to achieve high efficiency transmission of OAM beam by transmissive metasurface. In Ref. [39], a meta-FSS element based on the third-order band-pass filter is fabricated for OAM generation. Furthermore, a programmable transmissive metasurface is proposed with metal ring and PIN diode which can achieve OAM beam with $l = \pm1, \pm2$ modes at 5.35 GHz [40]. Recently, multi-OAM-beam has been realized in terahertz band in the existing literature. A method for multiplexing scheme of OAM in terahertz band was proposed by transmissive metasurface, which generates four vortex beams in different topological charges with incident Gaussian beam [41]. It is noted that the EM waves in terahertz band have the similar characteristics with that in optical band, which cannot exhibit the obvious diffraction phenomenon. Meanwhile, the incident Gaussian beam has well directivity for transmissive OAM generation but limited to the complex realization. In microwave band, the EM wave has strong diffraction phenomenon which is not conducive to the transmissive beam focusing due to the energy leaking effect. Therefore, the transmissive multi-OAM-beam is rarely reported in the band.

In this paper, a digital coding transmissive metasurface (DCTMS) in microwave band is proposed to OAM generation and the phase compensation is introduced for beam focusing. Three prototypes of DCTMS have been reported to generate the multi-OAM-beam with $l = -2$ modes based on PB phase. The unit cell of DCTMS is constructed of two metal bi-symmetrical arrow patches both are on side of single layer substrate. The single-, dual- and quad-OAM beams with $l = -2$ modes are generated based on the coding patterns by numerical simulations and provable experiments. The DCTMS may pave a way to application in multi-platform wireless systems.

2 Design and theoretical analysis

Schematic of muti-OAM-beam for DCTMS is demonstrated in Fig. 1(a). The different beams are manipulated by the varying coding sequences. A visualized illustration of DCTMS is shown in Figs. 1(b)–(e). The unit cell of DCTMS consists of a single layer substrate in the middle part and the two metallic bi-symmetrical arrow patches in both sides. The substrate is Rogers 4350B ($\varepsilon_r = 3.66$ and $\tan\delta = 0.0037$) with the thickness of 2.5 mm. The metal parts are made of copper with the conductivity of 5.8×10^7 S/m and the thickness of 0.036 mm. The optimized parameters are given as follows: $p = 10$ mm, $h = 2.5$ mm, $w = 1.08$ mm, $l = 7$ mm, $b_1 = 4.06$ mm, $\alpha = 130°$, $b_2 = 1.2$ mm, $m = 0.46$ mm.

For fulfilling the requirement of OAM phase, the transmissive elements should satisfy the high transmission coefficients and the phase shift of 360° simultaneously. The principle of PB phase has been introduced to reach continuous phase shift. It is applicable to coding multi-bit phase, whose phase is regulated by rotation of two metal bi-symmetrical arrow patches for unit cell. To elaborate the mechanism of PB phase, a right-hand circular polarization (RHCP) wave is incident along $-z$ direction. The electric field vector of incident wave $\boldsymbol{E}^i$ and transmissive wave $\boldsymbol{E}^t$ are expressed as

$$\begin{pmatrix} \boldsymbol{E}^i(\omega) \\ \boldsymbol{E}^t(\omega) \end{pmatrix} = \begin{pmatrix} E_0(\omega) & -\mathrm{i}E_0(\omega) \\ T_x E_0(\omega) & T_y E_0(\omega) \end{pmatrix} \begin{pmatrix} \boldsymbol{e}_x \\ \boldsymbol{e}_y \end{pmatrix}, \quad (1)$$

$$E_0(\omega) = |E_0(\omega)|\, \mathrm{e}^{-\mathrm{i}(kz+\omega t)}, \quad (2)$$

where T represents the transmissive coefficients of element. The phase shift of incident wave is expressed as

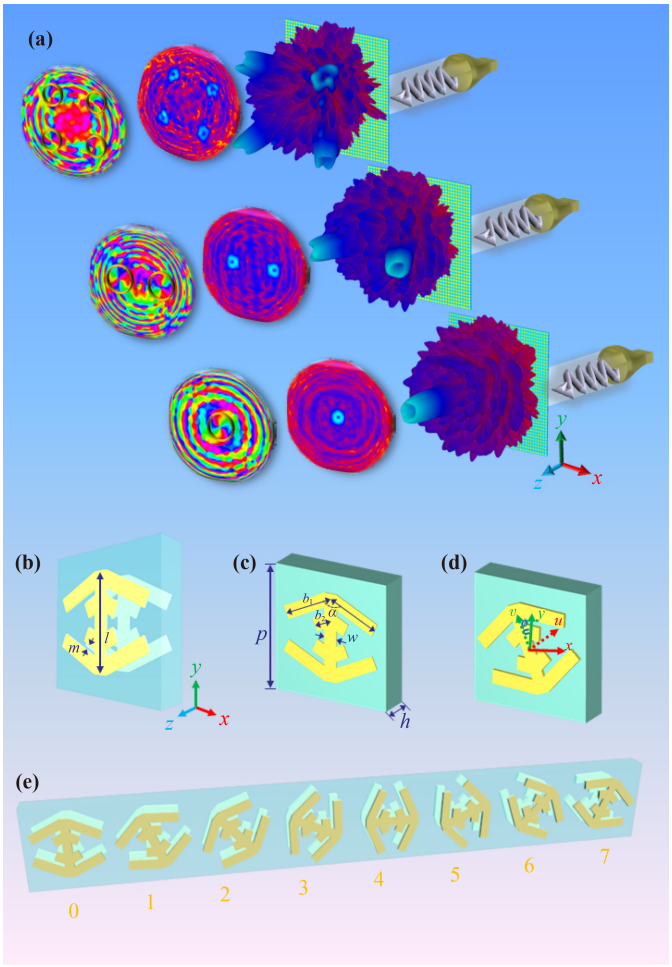

Fig. 1 Schematic of proposed DCTMS. **(a)** The visualized illustration of multi-OAM-beam of DCTMS with 40×40 coding unit cells. The single-OAM-beam, dual-OAM-beam and quad-OAM-beam with $l = -2$ mode are demonstrated by DCMTS with a linearly polarized horn antenna. **(b)** Perspective view of unit cell for DCTMS. **(c)** Bi-symmetrical arrow patches on the unit cell of DCTMS. **(d)** Bi-symmetrical arrow patches with rotating angle φ in u–v axis. **(e)** Schematic of 3bit digital coding elements for DCTMS.

Φ. The T_x and T_y are given as follows:

$$\begin{cases} T_x = |t_{xx}|\,\mathrm{e}^{-\mathrm{i}\Phi_{xx}} + |t_{yx}|\,\mathrm{e}^{-\mathrm{i}\Phi_{yx}} \\ T_y = |t_{yy}|\,\mathrm{e}^{-\mathrm{i}\Phi_{yy}} + |t_{xy}|\,\mathrm{e}^{-\mathrm{i}\Phi_{xy}} \end{cases}. \tag{3}$$

When the element rotates φ with respect to the y-axis, the incident electric field $\boldsymbol{E}^{ir}$ and transmissive electric field $\boldsymbol{E}^{tr}$ are respectively demonstrated in rotating u–v coordinate system as follows:

$$\begin{aligned} \begin{pmatrix} \boldsymbol{E}^{ir}(\omega) \\ \boldsymbol{E}^{tr}(\omega) \end{pmatrix} &= E_0(\omega) \begin{pmatrix} 1 & -\mathrm{i} \\ T_u & -\mathrm{i}T_v \end{pmatrix} \begin{pmatrix} \cos\varphi & -\sin\varphi \\ \sin\varphi & \cos\varphi \end{pmatrix} \begin{pmatrix} \boldsymbol{e}_u \\ \boldsymbol{e}_v \end{pmatrix} \\ &= E_0(\omega) \begin{pmatrix} e^{-\mathrm{i}\varphi} & -\mathrm{i}\mathrm{e}^{-\mathrm{i}\varphi} \\ T_u\mathrm{e}^{-\mathrm{i}\varphi} & -\mathrm{i}T_v\mathrm{e}^{-\mathrm{i}\varphi} \end{pmatrix} \begin{pmatrix} \boldsymbol{e}_u \\ \boldsymbol{e}_v \end{pmatrix}. \end{aligned} \tag{4}$$

Due to the element is irradiated with a circularly polarized wave, the transmissive phase shift and transmissive coefficients in u-axis have the equal tendency in x-axis, which means $\Phi_x = \Phi_u$ and $T_x = T_u$. The analogous results can be obtained that $\Phi_y = \Phi_v$ and $T_y = T_v$. Then transmissive wave $\boldsymbol{E}^{tr}$ in x–y coordinate system is expressed as

$$\begin{aligned} \boldsymbol{E}^{tr}(\omega) &= E_0(\omega) \begin{pmatrix} T_u\mathrm{e}^{-\mathrm{i}\varphi} \\ -\mathrm{i}T_v\mathrm{e}^{-\mathrm{i}\varphi} \end{pmatrix}^{\mathrm{T}} \begin{pmatrix} \cos\varphi & \sin\varphi \\ -\sin\varphi & \cos\varphi \end{pmatrix} \begin{pmatrix} \boldsymbol{e}_x \\ \boldsymbol{e}_y \end{pmatrix} \\ &= \frac{E_0(w)}{2} \begin{pmatrix} (T_x(w) - T_y(w))\,\mathrm{e}^{-\mathrm{i}2\varphi} \\ T_x(w) + T_y(w) \end{pmatrix}^{\mathrm{T}} \begin{pmatrix} \boldsymbol{e}_x + \mathrm{i}\boldsymbol{e}_y \\ \boldsymbol{e}_x - \mathrm{i}\boldsymbol{e}_y \end{pmatrix}. \end{aligned} \tag{5}$$

It is noted that $\boldsymbol{E}^t$ could be divided into two components including $\boldsymbol{E}^t{}_{(LHCP)}(\omega)$ and $\boldsymbol{E}^t{}_{(RHCP)}(\omega)$:

$$\boldsymbol{E}^t(\omega) = \boldsymbol{E}^t{}_{(LHCP)}(\omega) + \boldsymbol{E}^t{}_{(RHCP)}(\omega), \tag{6}$$

$$\begin{aligned} &\begin{pmatrix} \boldsymbol{E}^t_{(LHCP)}(\omega) \\ \boldsymbol{E}^t_{(RHCP)}(\omega) \end{pmatrix} = \frac{E_0(\omega)}{2} \\ &\cdot \begin{pmatrix} (|T_x(\omega)|\,\mathrm{e}^{\mathrm{i}\Phi_x} - |T_y(\omega)|\,\mathrm{e}^{\mathrm{i}\Phi_y})(\boldsymbol{e}_x + \mathrm{i}\boldsymbol{e}_y)\mathrm{e}^{-\mathrm{i}2\phi} \\ (|T_x(\omega)|\,\mathrm{e}^{\mathrm{i}\Phi_x} + |T_y(\omega)|\,\mathrm{e}^{\mathrm{i}\Phi_y})(\boldsymbol{e}_x - \mathrm{i}\boldsymbol{e}_y) \end{pmatrix}. \end{aligned} \tag{7}$$

When $|T_x(\omega)| = |T_y(\omega)| = |T(\omega)|$ and $|\Delta\Phi| = |\Phi_x - \Phi_y| = \pi$, Eq. (7) can be expressed as

$$\begin{aligned} &\begin{pmatrix} \boldsymbol{E}^t_{(LHCP)}(\omega) \\ \boldsymbol{E}^t_{(RHCP)}(\omega) \end{pmatrix} = \\ &\frac{1}{2}T(\omega)E_0(\omega) \begin{pmatrix} \mathrm{e}^{-\mathrm{i}2\varphi}(1 - \mathrm{e}^{\mathrm{i}(\pm\pi)})\,(\boldsymbol{e}_x + \mathrm{i}\boldsymbol{e}_y) \\ (1 + \mathrm{e}^{\mathrm{i}(\pm\pi)})\,(\boldsymbol{e}_x - \mathrm{i}\boldsymbol{e}_y) \end{pmatrix} \\ &= T(\omega)E_0(\omega) \begin{pmatrix} (\boldsymbol{e}_x + \mathrm{i}\boldsymbol{e}_y)\,\mathrm{e}^{-\mathrm{i}2\varphi} \\ 0 \end{pmatrix} \end{aligned} \tag{8}$$

From Eq. (1) to Eq. (8), it is concluded that only the LHCP component of transmissive wave has -2φ phase shift when it is irradiated by RHCP wave. To acquire perfect transmissive wave with circular polarization, the cross-polarized wave should be restrained which is available for co-polarized wave generation. Therefore, the co-polarized transmission t_{xx} and t_{yy} should be approximate to one while the phase difference of $\Delta\Phi = \Phi_{xx} - \Phi_{yy}$ could be close to 180°.

3 Simulated results and discussion

To obtain the continuous phase shift, the PB phase with 3bit is encoded by rotating the bi-symmetrical arrow patches. The rotating angle shifts from 0° to 180° with the step size of 22.5°. When the unit cell rotates with the angle of 0°, ±22.5°, ±45°, ±67.5°, ±90°, ±112.5°, ±135° ±157.5° successively, as a result, the transmissive phase response is dispersed into 8 particles including 0°, ±45°, ±90°, ±135°, ±180°, ±225°, ±270°,

±315°, which is noted as coding particles 0, 1, 2, 3, 4, 5, 6, 7. Figure 2 illustrates the simulated results of PB phase for unit cell. The transmissive coefficients under x- and y-polarized incident waves are demonstrated in Fig. 2(a). The transmission of $|t_{xx}| = |t_{yy}|$ in 9.2–9.4 GHz is higher than 0.8 and with the peak of 0.83 in 9.3 GHz. The phase difference is $\Delta\Phi = 180^{o}$ in highlight frequency band. In order to explain the mechanism of PB unit cell, t_{cp} is used to present the transmissive coefficients for circularly polarized incidence. RHCP and LHCP waves are indicated as + and – in subscript. It is observed that the amplitude of transmissive coefficients is near to 0.8 with circularly polarized incidence in Fig. 2(b), which illustrate the low energy loss. As given in Figs. 2(c) and (d), the transmissive phase response reveals 2φ periodic change with LHCP or RHCP incident waves when the unit cell rotates φ. The periodic change is coincident with PB phase principle. The double arrow structure is capable of achieving phase shift of 360deg and it can meet the requirement of PB phase metasurface.

In order to further explore the mechanism of proposed unit cell, the surface current distributions at 9.3 GHz are shown in Figs. S1(a)–(i) (Supporting information). The surface current is mainly affected by the metal bi-symmetrical arrow patches on both side of substrate as shown in Figs. S1(a)–(d) (Supporting information), which reveals the principle of PB phase metasurface. The spectrum in Figs. S1(e)–(i) (Supporting information) investigates the incident characteristics of proposed element, which demonstrates the wide-angle transmission.

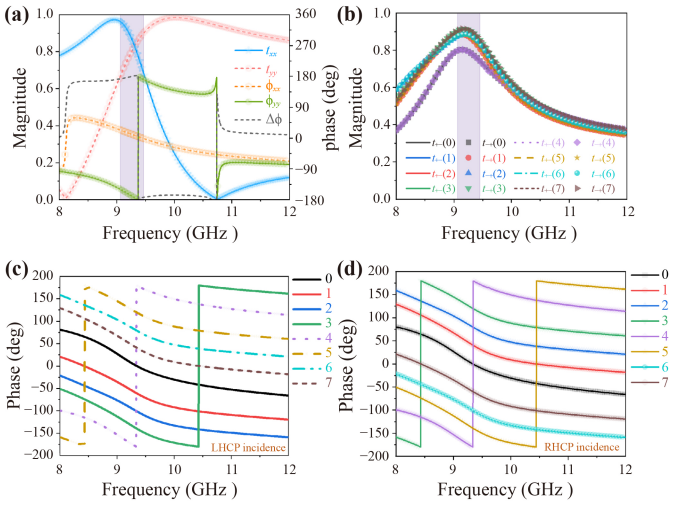

Fig. 2 The simulated results of PB phase for unit cell of DCTMS. **(a)** Amplitude and phase of transmissive coefficients with x- and y-polarized incident waves. **(b)** Amplitude of transmissive coefficients with different rotating angles for elements in LHCP and RHCP incident waves. **(c, d)** Phase of transmissive coefficients with different coding particles in LHCP and RHCP incidences.

The 3-bit PB phase digital coding transmissive metasurface with 40×40 unit cells has been proposed to achieve multi-OAM-beam. Generally, the spherical incident wave is not conducive to the transmissive beam focusing due to the energy leaking effect. Hence, DCTMS with horn antenna is introduced in Fig. 3(d). The horn antenna which generates the linearly polarized and spherical waves is located on one side of the metasurface. In order to simplify calculation, horn antenna has been seen as a point source. The origin of coordinates is on the upper layer of metasurface while the coordinates of horn antenna is $(0, 0, -z_f)$. It can be seen from Fig. 3(d) that the phase difference is mainly originated from the inequality distance between horn antenna and unit cells, the phase difference is calculated as follows:

$$\phi_{ij} = k_0(r_{ij} - z_f) = \frac{2\pi f_0}{c}\left(\sqrt{{x_i}^2 + {y_j}^2 + {z_f}^2} - z_f\right), \tag{9}$$

where k_0=2πf_0/c is expressed as the wave vector, f_0 presents the working frequency, r_{ij} is the distance between horn antenna and unit cell with coordinates (x_i, y_j, 0), and φ_{ij} is described as the compensational phase.

OAM is a phenomenon of vortex wavefront, it can be realized by an addition vortex phase factor exp(i$l\varphi$) for the Gaussian beam. The Gaussian beam will be converted into OAM beam by regulating phase of wavefront. The phase distribution is described as

$$\Phi(x, y) = l\varphi = l\arctan(y/x), \tag{10}$$

where l, as the topological charge, is the number of OAM mode. φ presents the azimuth angle. In this paper, we simulated and measured the results of OAM with mode $l = -2$. The results of OAM with mode $l = -2$ are shown in Fig. 3.

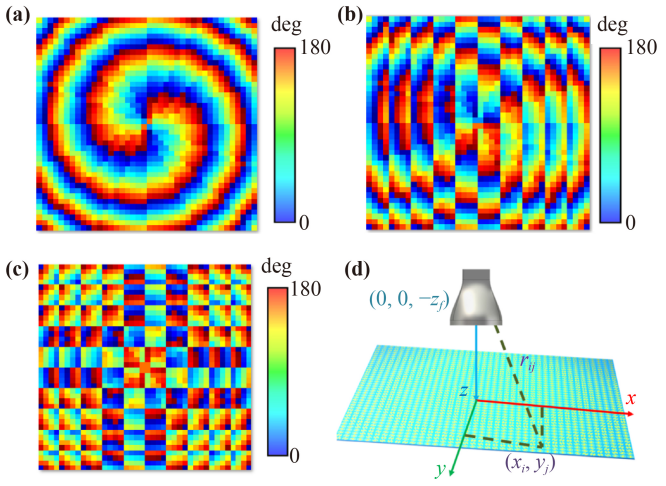

Fig. 3 Multi-OAM-beam with –2 mode for DCTMS. **(a)** Coding patterns of single-OAM-beam. **(b)** Coding patterns of dual-OAM-beam. **(c)** Coding patterns of quad-OAM-beam. **(d)** The coordinate system of DCTMS with horn antenna.

In order to satisfy the phase requirement, we need to add the compensational phase for spherical incidence in Fig. 3(d). The schematics of coding pattern for multi-OAM-beam are illustrated in Figs. 3(a)–(c). Furthermore, the schematics of three coding sequence process are exhibited in Fig. S2, Supporting information. The coding sequence of single-beam of OAM with –2 mode for DCTMS would be emerged by adding results of that with OAM and of compensational phase in Fig. 3(a). The coding sequence "44440000" varying from x-axis in Fig. 3(b) is applied for achieving two symmetrical OAM beams, where "4" and "0" represent the coding elements in Fig.1(e), respectively. The deflection angle of transmissive beam will be manipulated by the bit numbers of submatrix. It is calculated by Snell law as follows [43, 44]:

$$\theta = \arcsin(\lambda/\Gamma), \tag{11}$$

where $\lambda = 32.3$ mm corresponds to working frequency 9.3 GHz, and $\Gamma = 80$ mm presents the period length of submatrix. The equation manifests that the deflection angle will be controlled by the period length of submatrix for certain frequency. Afterwards it is calculated that the deflection angle is $\theta = 23.8$ deg with respect to z-axis.

The modulus coding sequence for quad-OAM-beam is shown in Fig. 3(c) which combines the coding sequence of beam split in two directions. The far-field pattern of quad-beam for OAM can be regarded as the symmetrical OAM beams in yOz-plane shifting to the plane of deflection beam along $+x$ direction and $-x$ direction. The elevation angle θ of modulus coding pattern can be calculated as

$$\theta = \arcsin(\sqrt{\sin^2\theta_1 + \sin^2\theta_2}), \tag{12}$$

where θ_1 and θ_2 present the deflection angles in x-axis and y-axis respectively. Both of them are 23.8° due to the same period length of coding submatrix. It is calculated that the elevation angel is $\theta = 34.0°$. The azimuth angle φ can be calculated as follows:

$$\varphi = \arctan\left(\frac{\sin\theta_2}{\sin\theta_1}\right). \tag{13}$$

Thus, the azimuth angle is calculated as $\varphi = 45°$, 135°, 225°, and 315° respectively.

The simulated magnitude and phase distributions of single-beam, dual-beam and quad-beam in spherical coordinate system are demonstrated in Figs. 4(a)–(c). It can be seen that the main beam of OAM displays energy leak in the center as shown in Fig. 4(a), which has vortex phase distribution corresponding to phase distribution in Fig. 4(b). The similar results are achieved at 9.2 GHz and 9.4 GHz as shown in Fig. S3, Supporting information.

Moreover, to observe perfect vortex distribution of OAM, the detection plane must be perpendicular to each OAM beam. Take quad-OAM-beam as example,

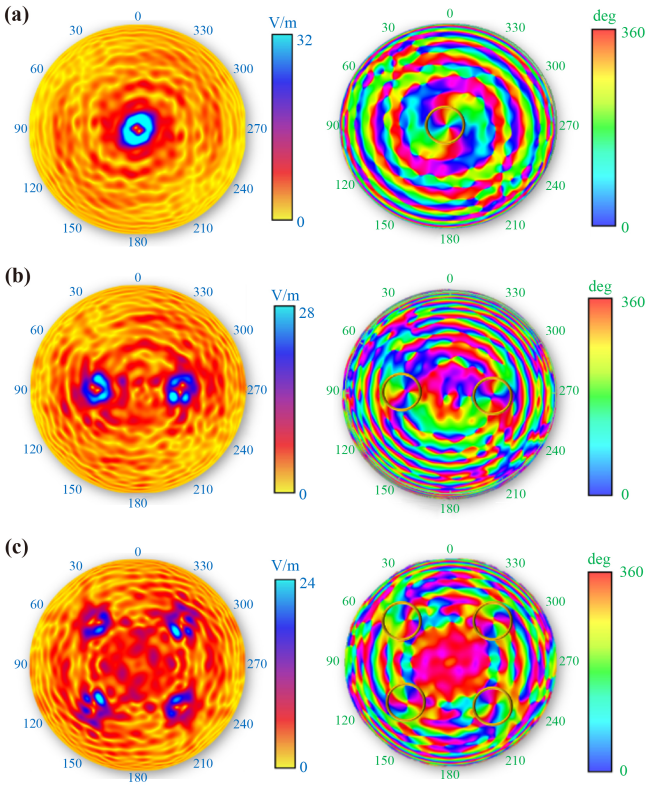

Fig. 4 Simulated magnitude and phase distributions of OAM beams. **(a)** Simulated magnitude and phase distributions of single-beam for OAM in spherical coordinate system. **(b)** Simulated magnitude and phase distributions of dual-beam for OAM in spherical coordinate system. **(c)** Simulated magnitude and phase distributions of quad-beam for OAM in spherical coordinate system.

the schematic of detection plane is demonstrated in Fig. 5(a). The simulated near-field distributions of single-OAM-beam, dual-OAM-beam and quad-OAM-beam are shown in Figs. 5(b)–(g). The distance between metasurface and detection plane for single-OAM-beam are 20 mm and that of dual-OAM and quad-OAM are 200 mm due to the inclination angle of beam. The magnitude distribution in Figs. 5(b, d, f) exhibits the characteristics of energy falling in the center of magnitude distribution. Meanwhile, the phase distribution is displayed the vortex phase distribution in in Figs. 5(c, e, g). The excellent quad-beam of OAM can be realized by the proposed DCTMS.

4 Fabrication and measurement

To corroborate the function, the prototypes of DCTMS are consisted of 1600 unit cells with the overall side of 400 mm × 400 mm, which are fabricated by standard print circuit board technique as shown in Fig. S4 (Supporting information). The free-space test method is employed in the measurement. Meanwhile, the schematic of far-field measurement environment is

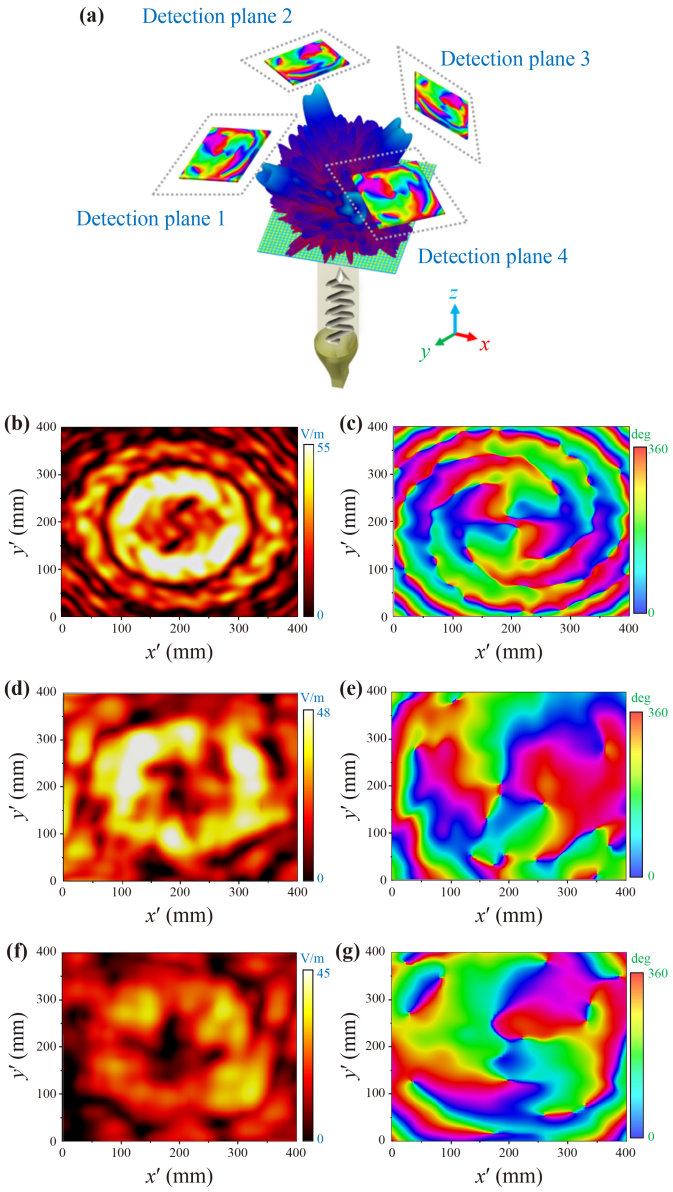

Fig. 5 The simulated results of near electric fields in 9.3 GHz. **(a)** Schematic of detection plane for quad-OAM-beam. **(b, d, f)** Simulated magnitude distributions of near electric fields in the perpendicular plane for one beam of DCTMS with single-OAM-beam, dual-OAM-beam and quad-OAM-beam. **(c, e, g)** Simulated phase distributions of near electric fields in the perpendicular plane for one beam of DCTMS with single-OAM-beam, dual-OAM-beam and quad-OAM-beam.

displayed in Fig. 6(a) and that of near-field is illustrated in Fig. 6(b). The experimental facilities include a vector network analyzer (Agilent N5230C), two standard-gain horn antennas and several RF coaxial cables. The launched horn antenna lays up to the center of the prototype with focal diameter ratio of 0.75 in the turntable and the received horn antenna is placed in another side to satisfy far-field condition. All the testing is fulfilled in a microwave anechoic chamber.

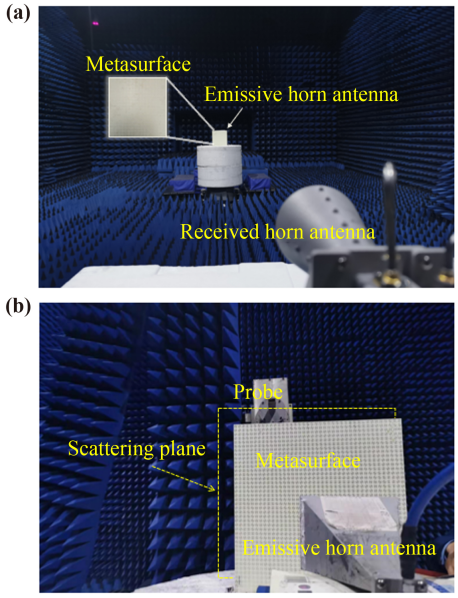

Fig. 6 Prototype of DCTMS for measurement environment in a microwave anechoic chamber. **(a)** The far-field measurement environment. **(b)** Near-field measurement environment.

In order to intuitively demonstrate the single-OAM-beam, dual-OAM-beam, quad-OAM-beam, the simulated far-filed patterns are illustrated in Figs. 7(a)–(c). It reveals that the gain of single beam can reach 17.8 dBi. The coding sequence "44440000" is tested and verified the function of dual-beam with the gain of 15.9 dBi in Fig. 7(b). The coding sequence "44440000" is recommended in Fig. S2(b) (Supporting Information). The coding sequences of dual-beam in *yOz*-plane and *xOz*-plane are combined and the far-field of chessboard coding sequences for quad-beam generation is given in Fig. 7(c). Similarly, the quad-OAM-beam is emerged with the gain of 14.2 dBi.

Experimental far-field radiation patterns of single-OAM-beam, dual-OAM-beam and quad-OAM-beam for DCTMS at 9.3 GHz are illustrated in Figs. 8(a)–(d). It can be found that the main beams emerge apparent energy falling characteristics. The deflect angles of dual-OAM-beam in Fig. 8(b) is about 23°. The gain of dual-OAM-beam with –2 mode is close to 15.45 dB which is coincided with the simulated results. Moreover, the quad-beam of OAM generated by DCTMS is located in different plane with azimuth angle of φ = 45°, 135°, 225°, 315°. The far-field patterns of OAM with –2 mode in the plane of φ = 45° and φ = 135° have been measured to realize all OAM beams in Figs. 8(c) and (d). It can be seen that the beam is symmetrical and deflects to different direction with angle of 34° and the gain is about 13.9 dB. Figures 8(e)–(j) illustrates the measured near-field results of single-OAM-beam, dual-OAM-beam and quad-OAM-beam for DCTMS at 9.3 GHz. The near-field magnitude distribution appears to cyclic annular feature which has low energy in the center, while the near-field phase distribution demonstrates the vortex property

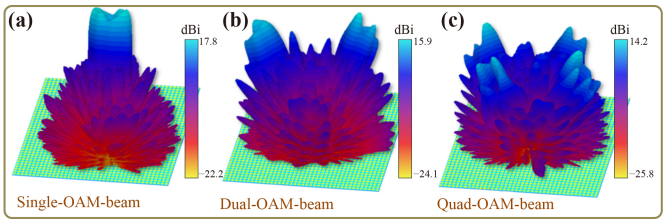

Fig. 7 Multi-OAM-beam with –2 mode for DCTMS. **(a)** Simulated far-field patterns of single-OAM-beam. **(b)** Simulated far-field patterns of dual-OAM-beam. **(c)** Simulated far-field patterns of quad-OAM-beam.

which shows the mode of $l = -2$ for OAM.

OAM purity is a significant concept to evaluate the performance of vortex beam. It can be calculated as follows based on Fourier-transform. The relationship is expressed as

$$A_l = \frac{1}{2\pi}\int_0^{2\pi} \psi(\varphi)\mathrm{d}\varphi \mathrm{e}^{-jl\varphi}, \tag{14}$$

$$\psi(\varphi) = \sum_l A_l \mathrm{e}^{jl\varphi}, \tag{15}$$

where A_l represents the mode weight of OAM spectrum with different mode l, $\psi(\varphi)$ is the angular distribution of OAM mode. Then the OAM purity is expressed as

$$\text{Mode purity} = \frac{{A_l}^2}{\sum {A_i}^2}. \tag{16}$$

Figures 9(a)–(c) respectively show the simulated and measured OAM purity of single-OAM-beam, dual-OAM-beam and quad-OAM-beam. It is illustrating that the simulated purity of single-OAM-beam, dual-OAM-beam and quad-OAM-beam with –2 mode is close to 97.6%, 88.3% and 77.3% respectively. Moreover, the measured OAM purity with –2 mode of single-, dual- and quad-beams is 93.8%, 83.9% and 70.4% for DCTMS prototypes. The experimental results agree well with the simulated dates. It is worth pointing that the OAM purity is relative to the beam numbers. The energy of main OAM beam has been dispersed and the weight of other topological charge increase with the beam number rising, which leads to the diminution of OAM purity.

To further illustrate the performance of proposed method, the OAM efficiency is introduced to reveal the transmission performance of OAM beams. For the transmissive metasurface, the OAM efficiency is a significant concept which is defined as the ratio of between the energy of transmissive OAM waves and that of incident wave, and it is defined as [45,46]

$$\eta = \frac{\int |\boldsymbol{E}_{\mathrm{RHCP}}|^2 \mathrm{d}s}{\int |\boldsymbol{E}_{\mathrm{in}}|^2 \mathrm{d}s} \times 100\%, \tag{17}$$

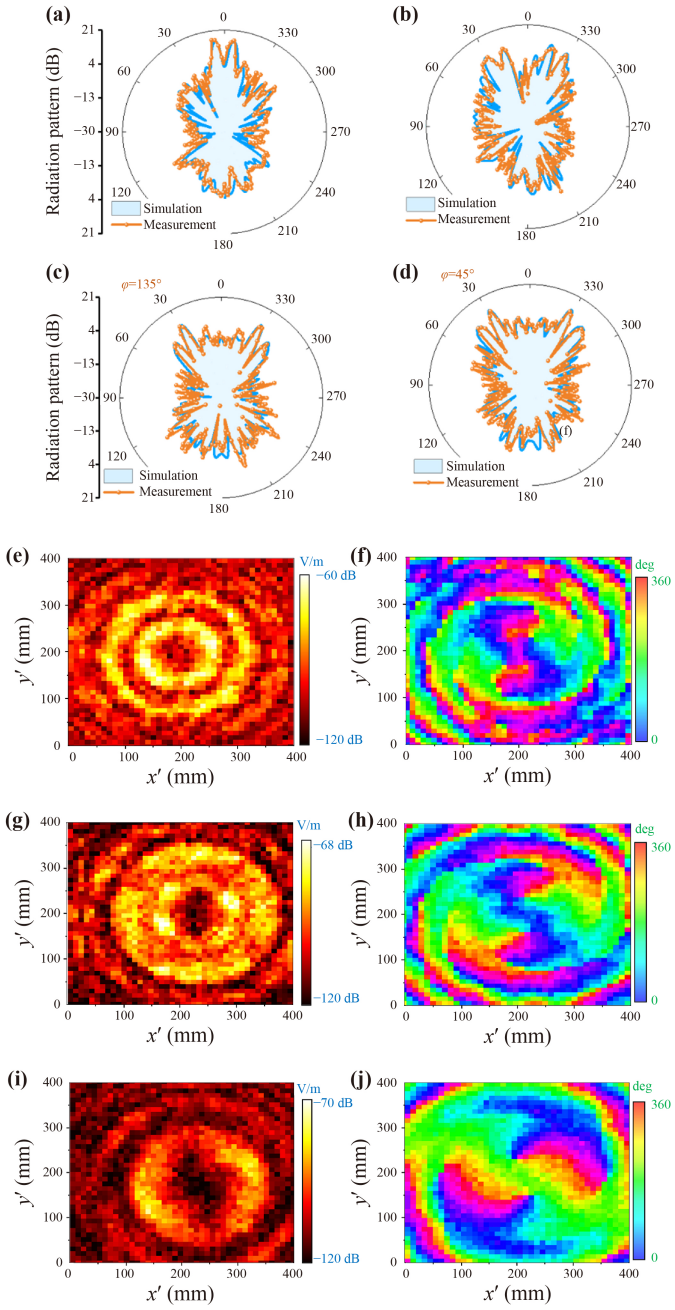

Fig. 8 Experimental and simulated results of DCTMS at 9.3 GHz. **(a)** Experimental and simulated far-field radiation patterns of single-OAM-beam. **(b)** Experimental and simulated far-field radiation patterns of dual-OAM-beam. **(c, d)** Experimental and simulated far-field radiation patterns of quad-OAM-beam when the azimuth angles are $\varphi = 45°$ and $\varphi = 135°$ respectively. **(e, g, i)** Experimental near-field magnitude distributions of single-OAM-beam, dual-OAM-beam and quad-OAM-beam with –2 mode at 9.3 GHz. **(f, h, j)** Experimental near-field phase distributions of single-OAM-beam, dual-OAM-beam and quad-OAM-beam with –2 mode at 9.3 GHz.

where E_{RHCP} is the electric vector of transmissive OAM field and E_{in} is that of incident field. Meanwhile, s is the integral area. Figure 9(d) reveals the OAM efficiency of proposed metasurface in 9.3 GHz. It can be found that

Table 1 Function comparison between our design with others in the literature.

Ref.	Type	Substrate layers	Working frequency	Incident polarization	Number of incidences	Generated polarization	Number of beams	Mode	Efficiency	OAM purity
[35]	RMS	single	microwave	LP	1	LP	2	1/2	—	—
[36]	RMS	three	terahertz	RHCP-GB	1	CP	4	1/2/3/4	—	—
[37]	RMS	single	microwave	LP	1	CP	4	2	—	—
[39]	TMS	dual	microwave	LHCP	1	CP	1	+2 +10/+20	80%	>93% >50%
[44]	RMS	single	microwave	LP	2	LHCP/ RHCP	4	±2/±1	—	—
[41]	TMS	single	terahertz	LP-/OAM-GB	2	LP	4	±2/±1	—	—
[43]	TMS	four	microwave	LP/LHCP/ RHCP	3	LP/LHCP/ RHCP	1	1/1.5/2/ 2.5/3	>60%	>83%
[45]	TMS	dual	microwave	LP	1	LP	1	+2/–2	—	>71%
This work	TMS	single	microwave	LP	1	RHCP	1	–2	88%	>93%
							2	–2	83%	>83%
							4	–2	73%	>70%

Note: TMS, Transmissive metasurface; RMS, reflective metasurface; GB, Gaussian beam; LP, linear polarization; CP, circular polarization.

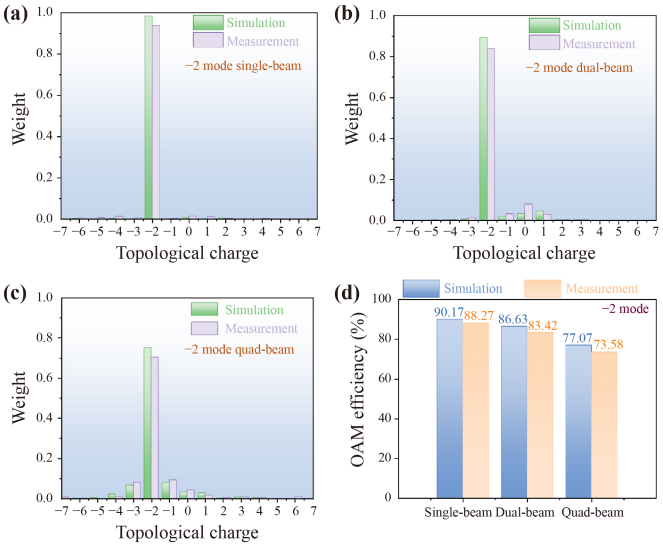

Fig. 9 Experimental and simulated spectrums of OAM purity and OAM efficiency for proposed trasnsmissive metasurface with different beams at 9.3GHz. **(a)** Spectrums of OAM purity for DCTMS with single-OAM-beam. **(b)** Spectrums of OAM purity for DCTMS with dual-OAM-beam. **(c)** Spectrums of OAM purity for DCTMS with quad-OAM-beam. **(d)** The OAM efficiency of single-OAM-beam, dual-OAM-beam and quad-OAM-beam.

the simulated OAM efficiency of –2 mode OAM for single-beam, dual-beam and quad-beam are 90.17%, 86.63% and 77.07%, It is indicated that the incident linear wave has been transmitted into OAM wave. The measured results are a bit lower than simulated results, which is the same as theoretical analysis. Consequently, the method for multi-OAM-beam generation is validated by experimental and simulated results, which reveals the excellent performance of the proposed DCTMS.

In comparison, Table 1 demonstrates the function between our design and others in the literature [35–37, 39, 41, 43, 46, 47]. The single linear polarized horn antenna is utilized in proposed method for multi-OAM-beam generation which has no complex feeding network and harsh test conditions at terahertz. The DCTMS is easy designed and fabricated. The method is simplifying the design process. Besides, the generated multi-OAM-beam has high purity by the designed structure and imteresting method. Furthermore, the single layer transmissive metasurface with multi-OAM-beam in microwave region has high efficiency and purity compared to the metasurfaces in Table 1 which reveals the well performance of proposed method.

5 Conclusion

In conclusion, the DCTMS are proposed to generate multi-OAM-beam. The metasurfaces for single-beam, dual-beam, and quad-beam of OAM with –2 mode are emerged by regulating coding pattern appropriately. Three prototypes are facilitated and measured in the microwave anechoic chamber. Moreover, the simulated and experimental results reveal the well performance of OAM which conforms to the predicted consequence. To further illustrate the performance of DCTMS, the OAM efficiency has been calculated which is higher than 73%. The OAM purity of proposed single-OAM-beam, dual-OAM-beam and quad-OAM-beam are close to 93%, 83% and 70%, respectively. The proposed method, which can be utilized to generate multi-beam OAM, is confirmed by theory analysis and experimental testing. It has potential application in the multi-platform wireless communication systems and the multi-channel imaging systems.

Electronic supplementary materials are available in the online version of this article at https://doi.org/10.1007/s11467-022-1179-9

and https://journal.hep.com.cn/fop/EN/10.1007/s11467-022-1179-9 and are accessible for authorized users.

Acknowledgements This work was supported by the National Natural Science Foundation of China (Grant Nos. 62171460 and 61801508), the Natural Science Basic Research Program of Shaanxi Province, China (Grant Nos. 2020JM-350, 20200108, and 20210110), the Young Innovation Team at Colleges of Shaanxi Province, China (Grant No. 2020022), the Postdoctoral Innovative Talents Support Program of China (Grant No. BX20180375), China Postdoctoral Science Foundation (Grant Nos. 2021T140111, 2019M650098, and 2019M653960), and the Postdoctoral Research Funding of Jiangsu Province (No. 2019K219).

Author contribution All the authors have accepted responsibility for the entire content of this submitted manuscript and approved submission.

Conflict of interest statement The authors declare no conflicts of interest regarding this article.

References

1. P. Zheng, Q. Dai, Z. Li, Z. Ye, J. Xiong, H. Liu, G. Zheng, and S. Zhang, Metasurface-based key for computational imaging encryption, *Sci. Adv.* 7(21), eabg0363 (2021)
2. X. Fang, H. Ren, and M. Gu, Orbital angular momentum holography for high-security encryption, *Nat. Photonics* 14(2), 102 (2020)
3. H. Sroor, Y. Huang, B. Sephton, D. Naidoo, A. Valles, V. Ginis, C. Qiu, A. Ambrosio, F. Capasso, and A. Forbes, Capasso Feder. and Forbes A., High-purity orbital angular momentum states from a visible metasurface laser, *Nat. Photonics* 14(8), 498 (2020)
4. S. Li, Z. Li, B. Han, G. Huang, X. Liu, H. Yang, and X. Cao, Multifunctional Coding Metasurface with Left and Right Circularly Polarized and Multiple Beams, *Front. Mater.* 9, 854062 (2022)
5. P. Feng, S. Qu, and S. Yang, OAM-generating transmitarray antenna with circular phased array antenna feed, *IEEE Trans. Antenn. Propag.* 68(6), 4540 (2020)
6. Q. Zhou, M. Liu, W. Zhu, L. Chen, Y. Ren, H. Lezec, and T. Xu, Generation of perfect vortex beams by dielectric geometric metasurface for visible light, *Laser Photonics Rev.* 15(12), 2100390 (2021)
7. J. Wang, S. Chen, and J. Liu, Orbital angular momentum communications based on standard multi-mode fiber, *APL Photonics* 6(6), 060804 (2021)
8. Q. Xiao, Q. Ma, T. Yan, L. W. Wu, C. Liu, Z. X. Wang, X. Wan, Q. Cheng, and T. J. Cui, Orbital–angular –momentum-encrypted holography based on coding information metasurface, *Adv. Opt. Mater.* 9(11), 2002155 (2021)
9. W. Chen, A. Zhu, J. Sisler, Z. Bharwani, and F. Capasso, A broadband achromatic polarization-insensitive metalens consisting of anisotropic nanostructures, *Nat. Commun.* 10(1), 1 (2019)
10. K. Ou, F. Yu, G. Li, W. Wang, A. E. Miroshnichenko, and W. Lu, Mid-infrared polarization-controlled broadband achromatic metadevice, *Sci. Adv.* 6(37), eabc0711 (2020)
11. S. Li, Y. Li, L. Zhang, Z. Luo, B. Han, R. Li, X. Cao, Q. Cheng, and T. Cui, Programmable controls to scattering properties of a radiation array, *Laser Photonics Rev.* 15(2), 2000449 (2021)
12. S. J. Li, B. W. Han, Z. Y. Li, X. B. Liu, G. S. Huang, R. Q. Li, and X. Y. Cao, Transmissive coding metasurface with dual-circularly polarized multi-beam, *Opt. Express* 30(15), 26362 (2022)
13. S. Li, T. Cui, Y. Li, C. Zhang, R. Li, X. Cao, and Z. Guo, Multifunctional and multiband fractal metasurface based on inter-metamolecular coupling interaction, *Adv. Theory Simul.* 2(8), 1900105 (2019)
14. Y. Tanaka, P. Albella, M. Rahmani, V. Giannini, S. A. Maier, and T. Shimura, Plasmonic linear nanomotor using lateral optical forces, *Sci. Adv.* 6(45), eabc3726 (2020)
15. B. Han, S. Li, Z. Li, G. Huang, J. Tian, and X. Cao, Asymmetric transmission for dual-circularly and linearly polarized waves based on a chiral metasurface, *Opt. Express* 29(13), 19643 (2021)
16. Z. Li, W. Liu, H. Cheng, D. Y. Choi, S. Chen, and J. Tian, Spin-selective full-dimensional manipulation of optical waves with chiral mirror, *Adv. Mater.* 32(26), 1907983 (2020)
17. Q. Song, S. Khadir, S. Vézian, B. Damilano, P. D. Mierry, S. Chenot, and P. Genevet, Bandwidth-unlimited polarization-maintaining metasurfaces, *Sci. Adv.* 7(5), eabe1112 (2021)
18. A. Dorrah, N. Rubin, A. Zai, M. Tamagnone, and F. Capasso, Metasurface optics for on-demand polarization transformations along the optical path, *Nat. Photonics* 15(4), 287 (2021)
19. S. Li, Y. Li, H. Li, Z. Wang, C. Zhang, Z. Guo, R. Li, X. Cao, and T. Cui, A thin self-feeding Janus metasurface for manipulating incident waves and emitting radiation waves simultaneously, *Ann. Phys.* 532(5), 2000020 (2020)
20. H. Lv, Q. Huang, X. Yi, J. Hou, and X. Shi, Low-profile transmitting metasurface using single dielectric substrate for OAM generation, *IEEE Antennas Wirel. Propag. Lett.* 19(5), 881 (2020)
21. Z. Zhang, Y. Zhang, T. Wu, S. Chen, W. Li, and J. Guan, Broadband RCS reduction by a quaternionic metasurface, *Materials (Basel)* 14(11), 2787 (2021)
22. F. Arute, K. Arya, R. Babbush, D. Bacon, J. C. Bardin, R. Barends, and J. M. Martinis, Quantum supremacy using a programmable superconducting processor, *Nature* 574(7779), 505 (2019)
23. A. Leitis, A. Heßler, S. Wahl, M. Wuttig, T. Taubner, A. Tittl, and H. Altug, All-dielectric programmable Huygens' metasurfaces, *Adv. Funct. Mater.* 30(19), 1910259 (2020)
24. X. Zhang, W. Jiang, H. Jiang, Q. Wang, H. Tian, L. Bai, and T. Cui, An optically driven digital metasurface for programming electromagnetic functions, *Nat. Electron.* 3(3), 165 (2020)
25. J. Zhao, X. Yang, J. Dai, Q. Cheng, X. Li, N. Qi, and T.

Cui, Programmable time-domain digital-coding metasurface for non-linear harmonic manipulation and new wireless communication systems, *Natl. Sci. Rev.* 6(2), 231 (2019)
26. L. Zhang, Z. Wang, R. Shao, J. Shen, X. Chen, X. Wan, and T. Cui, Dynamically realizing arbitrary multi-bit programmable phases using a 2-bit time-domain coding metasurface, *IEEE Trans. Antenn. Propag.* 68(4), 2984 (2020)
27. P. Xu, W. Jiang, X. Cai, S. Bai, and T. Cui, An integrated coding-metasurface-based array antenna, *IEEE Trans. Antenn. Propag.* 68(2), 891 (2020)
28. H. Li, Y. Li, J. Shen, and T. Cui, Low-profile electromagnetic holography by using coding Fabry–Perot type metasurface with in-plane feeding, *Adv. Opt. Mater.* 8(9), 1902057 (2020)
29. Z. Li, S. Li, B. Han, G. Huang, Z. Guo, and X. Cao, Quad-band transmissive metasurface with linear to dual -circular polarization conversion simultaneously, *Adv. Theory Simul.* 4(8), 2100117 (2021)
30. M. Tal, D. B. Haim, and T. Ellenbogen, Geometric phase opens new frontiers in nonlinear frequency conversion of light, *Front. Phys.* 17(1), 12302 (2022)
31. A. Karnieli, Y. Li, and A. Arie, The geometric phase in nonlinear frequency conversionn, *Front. Phys.* 17(1), 12301 (2022)
32. Y. Tian, X. Jing, H. Gan, C. Li, and Z. Hong, Free control of far-field scattering angle of transmission terahertz wave using multilayer split-ring resonators' metasurfaces, *Front. Phys.* 15(6), 62502 (2020)
33. H. Ahmed, H. Kim, Y. Zhang, Y. Intaravanne, J. Jang, J. Rho, S. Chen, and X. Chen, Optical metasurfaces for generating and manipulating optical vortex beams, *Nanophotonics* 11(5), 941 (2022)
34. Y. Bai, H. Lv, X. Fu, and Y. Yang, Vortex beam: generation and detection of orbital angular momentum, *Chin. Opt. Lett.* 20(1), 012601 (2022)
35. S. Yu, L. Li, G. Shi, C. Zhu, and Y. Shi, Generating multiple orbital angular momentum vortex beams using a metasurface in radio frequency domain, *Appl. Phys. Lett.* 108(24), 241901 (2016)
36. F. Yue, D. Wen, C. Zhang, B. D. Gerardot, W. Wang, S. Zhang, and X. Chen, Multichannel polarization-controllable superpositions of orbital angular momentum states, *Adv. Mater.* 29(15), 1603838 (2017)
37. L. Zhang, S. Liu, L. Li, and T. Cui, Spin-controlled multiple pencil beams and vortex beams with different polarizations generated by Pancharatnam–Berry coding metasurfaces, *ACS Appl. Mater. Interfaces* 9(14), 36447 (2017)
38. X. Bai, F. Zhang, L. Sun, A. Cao, C. He, J. Zhang, and W. Zhu, Dynamic millimeter-wave OAM beam generation through programmable metasurface, *Nanophotonics* 11(7), 1389 (2022)
39. Y. Wang, K. Zhang, Y. Yuan, X. Ding, B. Ratni, S. N. Burokur, and Q. Wu, Planar vortex beam generator for circularly polarized incidence based on FSS, *IEEE Trans. Antenn. Propag.* 68(3), 2938666 (2020)
40. X. Bai, F. Kong, Y. Sun, G. Wang, J. Qian, X. Li, A. Cao, C. He, X. Liang, R. Jin, and W. Zhu, High-efficiency transmissive programmable metasurface for multimode OAM generation, *Adv. Opt. Mater.* 8(17), 2000570 (2020)
41. H. Zhao, B. Quan, X. Wang, C. Gu, J. Li, and Y. Zhang, Demonstration of orbital angular momentum multiplexing and demultiplexing based on a metasurface in the terahertz band, *ACS Photonics* 5(5), 1726 (2018)
42. Y. Yuan, K. Zhang, B. Ratni, Q. Song, X. Ding, Q. Wu, and P. Genevet, Independent phase modulation for quadruplex polarization channels enabled by chirality-assisted geometric-phase metasurfaces, *Nat. Commun.* 11(1), 1 (2020)
43. K. Zhang, Y. Yuan, X. Ding, H. Li, B. Ratni, Q. Wu, and J. Tan, Polarization-engineered noninterleaved metasurface for integer and fractional orbital angular momentum multiplexing, *Laser Photonics Rev.* 15(1), 2000351 (2020)
44. G. Ding, K. Chen, N. Zhang, J. Zhao, T. Jiang, and Y. Feng, Independent wavefront tailoring in full polarization channels by helicity-decoupled metasurface, *Ann. Phys.* 534(4), 2100546 (2022)
45. Y. Pan, F. Lan, Y. Zhang, H. Zeng, L. Wang, T. Song, and Z. Yang, Dual-band multifunctional coding metasurface with a mingled anisotropic aperture for polarized manipulation in full space, *Photon. Res.* 10(2), 416 (2022)